Coupled Electromagnetic and Reaction Kinetics Simulation of Super-Resolution Interference Lithography

Adela Habib,[†,¶] Harikrishnan Vijayamohanan,[‡,¶] Chaitanya K. Ullal,[*,‡] and Ravishankar Sundararaman[*,‡,†]

[†]*Department of Physics, Applied Physics and Astronomy, Rensselaer Polytechnic Institute, Troy, NY 12180, USA*
[‡]*Department of Materials Science and Engineering, Rensselaer Polytechnic Institute, Troy, NY 12180, USA*
[¶]*These authors contributed equally*

E-mail: ullalc@rpi.edu; sundar@rpi.edu

Abstract

Inspired by the ability of super-resolved fluorescence microscopy to circumvent the diffraction barrier, two-color super-resolution interference lithography exploits non-equilibrium kinetics in materials to achieve large area nanopatterning while using visible light. Periodic patterns with super-resolved features down to tens of nanometers have been demonstrated in thin films and monolayers. Extending these advances to the bulk nanopatterning of thick films requires a quantitative understanding of the time-dependent interactions of optical dynamics, including absorption, diffraction and intensity modulation at two wavelengths, with the photo-activated and inhibited reaction kinetics. Here, we develop an efficient electromagnetic (EM) perturbation theory approach that facilitates for the first time fully-coupled simulations of EM and chemical kinetics in two-color interference lithography. Applied to a spirothiopyran-functionalized photoresist system, these simulations show that diffraction and absorption effects are negligible ($< 0.1\%$) for depths up to 10 μm, and that tuning exposure time and intensities can lead to concentration contrasts up to 80%. We investigate multiple exposure strategies to reduce pitch of the line pattern including sequential exposures with different times to achieve uniform lines, and multiplexed exposures with equal periods. This capability to rapidly and accurately predict the coupled optical and chemical dynamics facilitates computational design of high-precision patterns in two-color interference lithography.

Introduction

Additive manufacturing is increasingly making the transition from rapid prototyping to industrial adoption in fields as diverse as aviation, construction, sportswear and medical devices. In the specific case of photopolymerization based 3D printing, the first additive manufacturing method to be adopted by industry, this trend is only projected to grow, fueled by recent advances in high throughput fabrication on the order of cubic meters of volume in a few hours.[1,2]

Separately, emergent nanotechnologies require the development of lithography tools that can operate in 3 dimensions with high resolutions.[3,4] Within the context of direct writing with focused visible light, diffraction is a key barrier that limits feature size. The diffraction limit has been overcome in far field optical microscopy using reversibly photoswitchable systems.[5] These principles have in turn been applied to direct write lithography.[6–9] Such "super-resolution" lithography techniques involve light-driven activation and inhibition, with the spatial variation in the intensity ratio between the two colors (activation and inhibition frequencies) leading to crosslinked features below the diffraction limit.[10] Unfortunately, the high exposure doses needed in many of these systems has meant that fabrication speed remains a challenge.[11] It is worth noting that apart from far-field super-resolution lithography, near field techniques such as surface plasmon interference lithography have been developed for large area nanopatterning, albeit in 2D.[12,13]

Two color photoresists with inhibition intensity thresholds that are several orders of magnitude lower[10,14] can be used in interference lithography configurations that involve the exposure of a photosensitive medium to two or more coherent beams of light. Interference lithography is inherently configured to support large area coverage, albeit at the cost of being restricted to periodic patterns.[15–17] Feature sizes on the order of tens of nanometers have been demonstrated while using visible light in super resolution inspired interference lithography configurations.[18–20]

The throughput benefits of interference lithography are far greater when the patterns are not limited to a single planar layer.[21] This extension of super-resolution interference lithography into the third dimension is non-trivial due to the large number of process parameters involved. The parameters that must be optimized include not just those that are directly related to the simultaneous interaction of the two colors of light with the photoresist, but resist-developer interactions, and the mechanical properties of the resultant structures, including during the drying process. Decoupling these processes to gain insight into the impact of individual

process parameters is experimentally challenging. It is unsurprising that the simulation of conventional (single-color) interference lithography played an important role in optimizing exposures and photoresist chemistry.[22–24] Corresponding advances in two-color lithography are needed to establish a comprehensive understanding of the coupled effects of optical dynamics including absorption, diffraction and intensity modulation at two wavelengths, along with the competitive photo-activated and inhibited reaction kinetics within the resists. There is, thus, a strong need for simulation tools that can quantitatively predict the interactions between the optics and chemistry in the super resolution interference writing process.

Simulating super-resolution interference lithography requires the coupled time evolution of spatially-varying chemical concentration profiles $C_\alpha(\mathbf{r},t)$ of several species and optical intensity profiles at two wavelengths: $I_1(\mathbf{r},t)$ for the activation and $I_2(\mathbf{r},t)$ for inhibition, as shown in Figure 1. The goal is to evolve the coupled kinetics and electromagnetic (EM) intensities in time, given initial concentrations in the resist and a configuration of laser sources. The intensities I_1 and I_2, which depend on the chemical concentrations throughout the simulation domain, must be obtained at each point in the simulation domain by an EM simulation for each time step. These intensities then determine the rate of change of chemical concentrations that are in turn determined by the chemical kinetics particular to the photo-resist in consideration. Unfortunately, conventional finite-difference time-domain or finite-element methods for solving the EM equations are too computationally expensive to incorporate into every time step of a kinetics simulation. This is particularly exacerbated by the stiffness of the differential equations that govern the chemical kinetics, necessitating small time steps that amount to solving the EM wave equations $\sim 10^4$ times in each simulation that we present below.

Here, we demonstrate the ability to efficiently capture and investigate the coupled electromagnetic and reaction kinetics in non-planar patterns of two color super-resolution interference lithography. A key advance is the first step, in which we develop and benchmark a perturbative EM simulation technique that rapidly predicts interference and intensity modulation due to the spatially periodic variation in absorption in the resist. We then incorporate the intensity from this EM approach applied to two wavelengths in a self-consistent solution of the time-dependent chemical kinetics in the resist. We apply this technique over 2D simulation domains to gain insight into the fabrication of sub-wavelength lines using a spirothiopyran-based resist chemistry that is designed for super-resolution interference lithography.[14,19,25] Specifically, we investigate the deleterious effects of absorption and diffraction, the impact of varying intensity ratios and exposure times, the performance of standing waves in both colors compared to standing wave in only the inhibition beam, and different approaches to writing lines with sub-diffraction spacing using multiple exposures.

Methods

Chemical kinetics

For definiteness, we focus on a spirothiopyran functionalized photoresist which was designed with the objective of enabling large-volume interference lithography by virtue of its low threshold intensity for inhibition. This reaction system is summarized in Fig. 1 with overall kinetics given by

$$\begin{aligned}
\dot{C}_{\mathrm{SP}} &= C_{\mathrm{MC}}\left(\kappa + (I_1 e_1^{\mathrm{MC}} + I_2 e_2^{\mathrm{MC}})\phi_r\right) - C_{\mathrm{SP}} I_1 e_1^{\mathrm{SP}} \phi_f \\
\dot{C}_{\mathrm{MC}} &= -C_{\mathrm{MC}}\left(\kappa + (I_1 e_1^{\mathrm{MC}} + I_2 e_2^{\mathrm{MC}})\phi_r\right) + C_{\mathrm{SP}} I_1 e_1^{\mathrm{SP}} \phi_f \\
&\quad - k_3 C_{\mathrm{MC}} C_{\mathrm{Atto}} \\
\dot{C}_{\mathrm{MAP}} &= k_3 C_{\mathrm{MC}} C_{\mathrm{Atto}}, \qquad (1)
\end{aligned}$$

where $C_\alpha(\mathbf{r},t)$ and $\dot{C}_\alpha(\mathbf{r},t)$ are the concentrations and time derivatives of various species α = MC, SP, MAP and Atto discussed below, $I_{1,2}(\mathbf{r},t)$ are the intensity profiles, $e_{1,2}^\alpha$ are the extinction coefficients of each species at each wavelength, and ϕ_r, ϕ_f, k_3 and κ are rate constants. Note that the intensities and concentrations depend on space and time (omitted above for clarity), while all other parameters are constants specific to the photo-resist that have been experimentally measured and tabulated in Ref. 19.

Briefly, this reaction system involves an activation process (rate constant ϕ_f) by UV light with wavelength $\lambda_1 = 366$ nm and intensity I_1 which converts spirothiopyran (SP) to its merocyanine isomer (MC). The reverse reaction (rate constant ϕ_r) is predominantly driven by the inhibiting green light with wavelength $\lambda_2 = 532$ nm and intensity I_2, in addition to I_1 and a thermally-activated process with rate constant κ. The MC isomer can react with maleimide moieties (Atto) in the resist via an irreversible Thiol-Michael addition reaction (rate constant k_3) to form the final crosslinked product (MAP). The goal in interference lithography is then to control these reactions by spatially modulating I_1 and I_2 to achieve a specific concentration profile C_{MAP} of the final 'written' product. See Ref. 19 for further details of the reaction kinetic model and their parameter calibration.

Electromagnetic wave propagation

In order to determine $C_\alpha(\mathbf{r},t)$ by solving (1), we need to solve the EM wave equations to find the instantaneous intensity profiles $I_1(\mathbf{r},t)$ and $I_2(\mathbf{r},t)$ at *each time step*. To circumvent the aforementioned impracticality of using conventional finite-difference time-domain or finite-element methods for this task, we formulate a perturbative approach to calculate the intensity modulation and diffraction effects, which is possible because the absorption due to the spatially varying concentration profiles is relatively small. Specif-

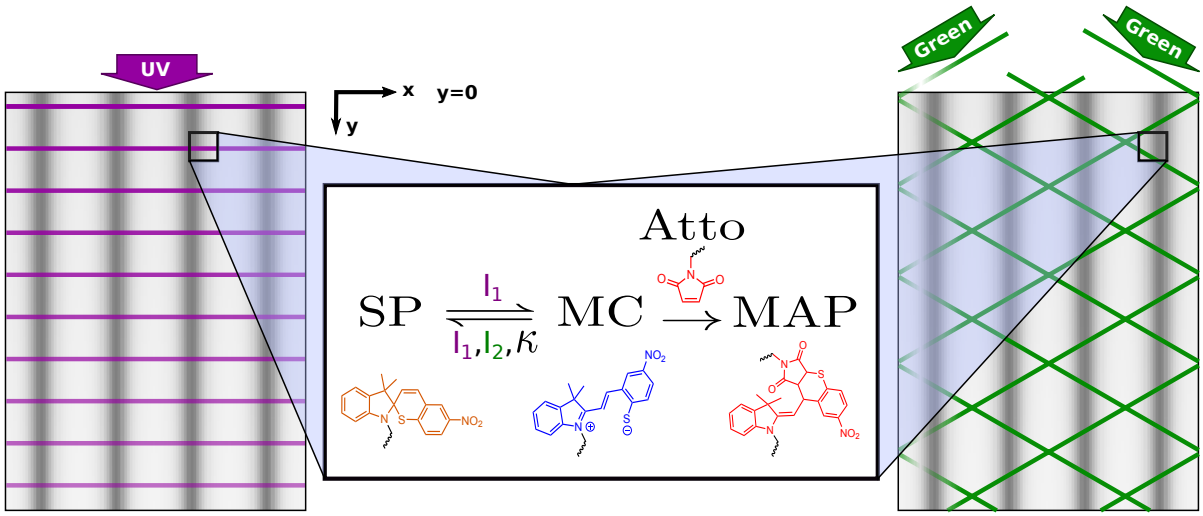

Figure 1: Simultaneous illumination by an activating UV plane wave (I_1) and an inhibiting green standing wave (I_2) drives reactions between spirothiopyran (SP), its reactive photoisomer merocyanine (MC), and maleimides (Atto), to produce the final Michael addition product (MAP) in a sub-diffraction line pattern shown as dark grey vertical bars. We perform chemical kinetics simulations of the line formation with the intensity diffraction pattern of both light fields updated self-consistently at each time step of the simulation.

ically, the resist has a dielectric function $\epsilon_{1,2}(\mathbf{r},t) = \epsilon_b(1 + i\eta_{1,2}(\mathbf{r},t))$ (at the two relevant wavelengths λ_1 and λ_2). Here, $\epsilon_b \approx 2.10$ is the approximately spatially-invariant dielectric constant of the solution and $\eta(\mathbf{r},t) = \sum_\alpha C_\alpha(\mathbf{r},t)e^\alpha_{1,2}\ln(10)\lambda_{1,2}/(2\pi\sqrt{\epsilon_b})$ is the spatially-dependent loss tangent (written in terms of the extinction coefficients of each species).

For each wavelength (λ_1 and λ_2), we need to solve Maxwell's equations in a charge-free and non-magnetic medium

$$\nabla \cdot \epsilon(\mathbf{r})\frac{\partial \mathbf{A}}{\partial t} = 0$$
$$\nabla \times (\nabla \times \mathbf{A}) = \mu_0 \mathbf{j} - \mu_0\epsilon_0\epsilon(\mathbf{r})\frac{\partial^2 \mathbf{A}}{\partial t^2} \qquad (2)$$

where $\mathbf{A}$ is the vector potential and $\mathbf{j}$ is the current density of the source. Note that while $\epsilon(\mathbf{r})$ changes in time during the chemical kinetics evolution above (on seconds - minutes time scales), it is constant at the electromagnetic oscillation time scale (femtoseconds). Focusing on the line geometry for this initial study, we can work with a 2D domain spanning x (periodicity direction) and y (depth into the film), with all quantities invariant with z, which is the line direction as well as the direction of the electric field and vector potential. In this transverse electric (TE) polarization geometry and using the Coulomb gauge, only $A_z(x,y)$ is non-zero, which reduces Eq. (2) to

$$(\nabla^2 + k^2(1 + i\eta(\mathbf{r})))A_z(\mathbf{r}) = -\mu_0 j_z(\mathbf{r}), \qquad (3)$$

where $k = 2\pi\sqrt{\varepsilon_b}/\lambda$ is the magnitude of the wavevector in the uniform medium (without dissipation).

The sources $j_z(\mathbf{r})$ and the concentration profile $C_\alpha(\mathbf{r})$ are all periodic in x with period L_x for the standing wave patterns utilized.[1] We solve these equations with periodic boundary conditions in x and non-reflective boundary conditions in y (assuming an index-matched substrate to avoid reflections) over a domain of dimensions $L_x \times L_y$. Using this periodicity, we can expand the source current, loss tangent and vector potentials in a Fourier series in x. The source current may be localized to the boundary $y = 0$ as $j_z(\mathbf{r}) = -J_0\delta(y)e^{2\pi n_0 ix/L_x}$, where $n_0 = 0$ for a plane wave source and $n_0 = 1$ for a standing wave source with the periodicity of the desired line pattern. For the loss tangent and vector potential, we expand $\eta(\mathbf{r}) = \sum_m \eta_m(y)e^{2\pi mix/L_x}$ and $A_z(\mathbf{r}) = \sum_n A_n(y)e^{2\pi nix/L_x}$. Substituting these expansions, Eq. (3) reduces to a set of coupled 1D differential equations indexed by n,

$$\left(\partial_y^2 - \left(\frac{2\pi n}{L_x}\right)^2 + k^2(1 + i\eta_0(y))\right)A_n(y) + \sum_{m\neq 0} ik^2\eta_m(y)A_{n-m}(y) = J_0\delta(y)\delta_{nn_0}, \qquad (4)$$

where we have separated the x-averaged loss tangent $\eta_0(y)$ which contributes to overall attenuation of the lasers from the remaining Fourier components which lead to diffraction.

The perturbative solution to the EM equation Eq. (3) relies on the spatially varying loss tangents being small, $|\eta| \ll 1$. We treat the overall attenuation due to $\eta_0(y)$ exactly, while treating remaining Fourier components ($\eta_{m\neq 0}$) perturbatively. In this treatment, the zeroth order wave $A^{(0)}$ is only at the Fourier component of the

[1] Note that the lines will be at separation $L_x/2$ following the periodicity of the intensity, which is the square of the electric field with periodicity L_x.

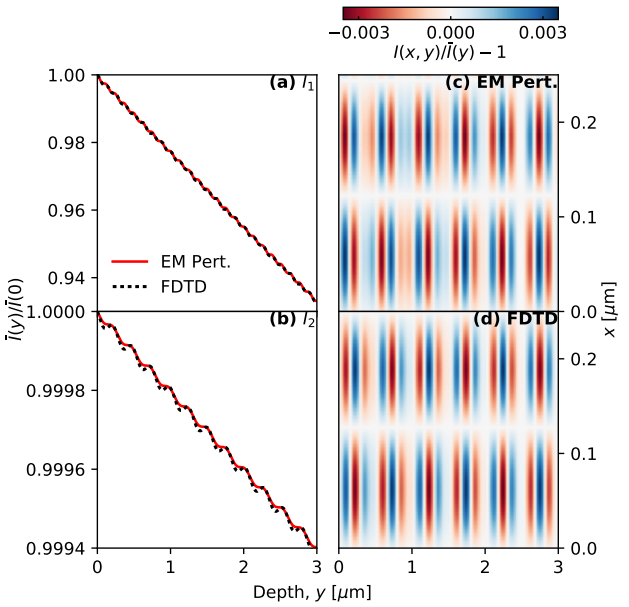

Figure 2: Intensities predicted by electromagnetic (EM) perturbation theory agree quantitatively (error $< 0.05\%$) with finite difference time domain (FDTD) simulations for the x-averaged intensity $\bar{I}(y)$ attenuation of (a) activation UV light and (b) inhibition green light, as well as (c,d) the relative deviations from $\bar{I}(y)$ due to diffraction (shown for the UV light which is absorbed and diffracted more strongly).

source ($n = n_0$),

$$\left(\partial_y^2 - \left(\frac{2\pi n_0}{L_x}\right)^2 + k^2(1 + i\eta_0(y))\right) A_{n_0}^{(0)}(y) = J_0\delta(y). \tag{5}$$

The second term in Eq. (4) serves as a source for the remaining Fourier components of the wave at first order $A^{(0)}$,

$$\left(\partial_y^2 - \left(\frac{2\pi n}{L_x}\right)^2 + k^2(1 + i\eta_0(y))\right) A_n^{(1)}(y) = -ik^2\eta_{n-n_0}(y)A_{n_0}^{(0)}(y), \tag{6}$$

which then captures diffraction effects. Note that coupling between $n \neq n_0$ components are at second and higher order, which we neglect in this perturbative treatment.

We solve the 1D differential equation using a finite-difference discretization that reduces it to a tridiagonal matrix equation. For $n = n_0$, we set $A_0^{(0)}(0) = \sqrt{I_0}$ to correspond to incident intensity,[2] and set a no incoming wave boundary condition at $y = L_y$. For $n \neq n_0$, we set no-incoming-wave boundary conditions at both $y = 0$ and L_y. For each time step of the kinetics problem, we construct $\eta(x, y)$ on a uniform grid from the concentration profiles, perform a Fast Fourier transform (FFT) along the x direction to get $\eta_m(y)$, calculate $A_n(y)$ using a sequence of tridiagonal matrix solves as discussed above, and then inverse FFT along x to get $A_z(x, y)$ and the intensity $I(x, y) = |A_z(x, y)|^2$.

Fig. 2 shows that the resulting intensity from the perturbative EM method is in excellent agreement with finite-difference time-domain (FDTD) simulations using the MEEP software[26] carried out on a characteristic loss tangent profile (based on the simulations below). Both the planarly-averaged intensity attenuation and the detailed modulation of the intensity are in excellent agreement, with the overall error in the intensity profile $< 0.05\%$. The perturbative method requires only 0.005 core-seconds for this test calculation compared to 50 core-minutes for FDTD. This allows us to integrate this simulation into the chemical kinetics solver which evaluates $\sim 10^4$ time steps for the results shown below.

Computational details

The chemical kinetics evolution employs an embedded Runge-Kutta 4-5 order integrator with adaptive step size control[27] applied to a vector of concentrations $C_\alpha(\mathbf{r})$ over a uniform grid, with $I_1(\mathbf{r})$ and $I_2(\mathbf{r})$ treated as dependent variables recalculated each time. The initial concentrations are $C_{\mathrm{SP}} = C_{\mathrm{Atto}} = 0.01$ mol/liter (corresponding to a polyethylene glycol photoresist comprised of 5% SPT by weight with a swelling ratio of 10) and $C_{MC} = C_{\mathrm{MAP}} = 0$,[19] that is uniform in the simulation domain. The converged grid resolution is 100 points per micron, with $L_x = 0.26\mu$m for the chosen standing wave geometry resulting in concentration profiles with the same periodicity, and film thickness L_y varied up to 20 μm. We keep the source geometry constant in the remainder of this study, and explore the dependence of the obtained concentration profiles on film thickness (depth L_y), intensity and exposure times.

We note that in one dimensionally periodic structures with features on the order of 100 nm or less, the larger film thicknesses, such as 20μm, would result in impractical feature aspect ratios of greater than 100:1. Nevertheless, understanding the impact of attenuation and diffraction effects even for large thicknesses is useful. While practical implementations of one and two dimensional structures would utilize only the smaller thicknesses from the results presented, the trends and physical insights for larger thicknesses are particularly relevant to multi-beam interference patterns that result in three dimensional structures that are self supporting and continuously connected.[15,16,21]

Figure 3(a) shows the concentration profile of the final MAP product in a typical simulation corresponding to 1000 s exposure time at intensities $I_1 = 6 \times 10^{-4}$ and $I_2 = 1$ mol/m^2 of photons (used throughout below, except where specified otherwise).[19] We compute two metrics to quantify the uniformity of the polymer written after a specific exposure condition. First, we characterize a typical line width by computing the ex-

[2] For notational convenience, we have absorbed prefactors of ϵ_0, c and ω into the definition of A so that we can write intensity as $I = |A|^2$.

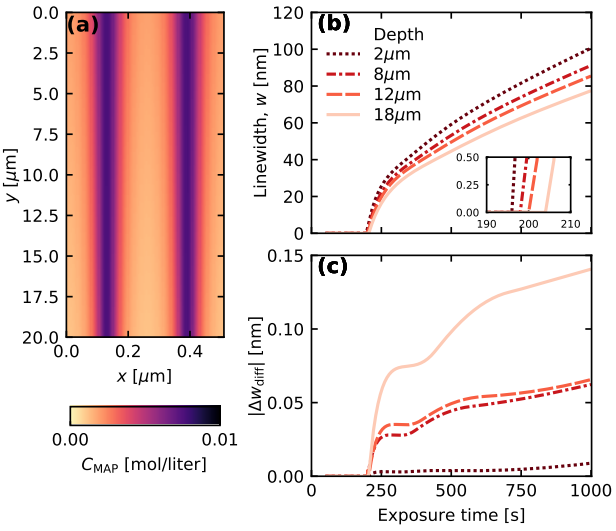

Figure 3: (a) Concentration profile of the Michael addition product (MAP) after 1000 s of exposure. (b) Calculated linewidths, w, and (c) change of linewidths, $|\Delta w_{\text{diff}}|$ due to diffraction beyond overall attenuation of the beam, as a function of exposure time at a few selected depths. The inset in (b) shows that the lines appear at slightly different times for the selected depths. Line widths decrease slightly with depth due to attenuation of the activation UV laser, and diffraction effects are negligible.

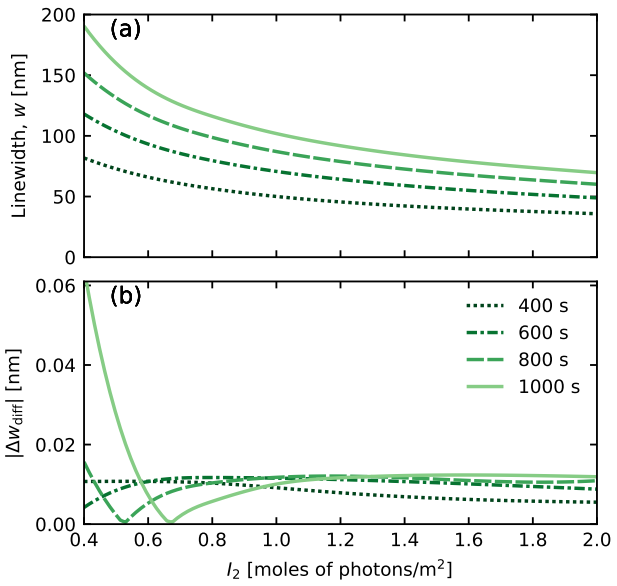

Figure 4: (a) Calculated linewidths, w, at the top of the film and (b) change of linewidths due to diffraction, $|\Delta w_{\text{diff}}|$, as a function of the intensity of the inhibiting green standing waves at a few selected exposure times. Line widths can be increased by either increasing exposure time or reducing I_2, and diffraction effects are minimal throughout.

tent of x at a given depth y for which the concentration $C_{\text{MAP}}(\mathbf{r}) \geq C_0$, where the threshold C_0 is a concentration of MAP above which the polymer will not wash away. This threshold can be altered by controlling the cross-link density of the polymer, and for definiteness, we set $C_0 = 0.005$ mol/liter, which corresponds to the gel point of a trifunctional monomer at the given initial concentration.[28] Additionally, we calculate the concentration contrast similar to Michaelson contrast for an interference pattern.,[29]

$$\text{Contrast} = \frac{\max C_{\text{MAP}}(\mathbf{r}) - \min C_{\text{MAP}}(\mathbf{r})}{\max C_{\text{MAP}}(\mathbf{r}) + \min C_{\text{MAP}}(\mathbf{r})}. \quad (7)$$

Experimentally, the target would be to achieve a desired line width uniformly through the depth of the film, with as high a concentration contrast as possible (low concentration of crosslinked polymer networks at intended nodes).

Results & Discussion

Attenuation and diffraction effects

Attenuation of the laser light due to absorption by the photoresist invariably leads to non-uniformity of line widths and decreasing concentration contrast at increasing depths.[8,19] We therefore leverage our simulation framework to identify the theoretical limits of uniformity with depth for the chosen spirothiopyran two-color lithography chemistry. Figure 3(b) shows the line width at various depths as a function of exposure time, while accounting for the impact of changes in concentration and dielectric constant. The lines begin to first appear at times that correspond to the point when C_{MAP} first exceeds C_0 in the minima of the inhibiting green standing waves. Although these times vary monotonically as a function of depth, they are all close to 200 s of exposure, as can be seen from the inset in Fig. 3(b). With increasing depth, attenuation primarily affects the activating UV beam (Fig. 2), resulting in a reduction of line width of approximately 10% and 25% at 8 μm and 18 μm depth respectively relative to the top of the film.

Figure 3(c) shows the effect of diffraction beyond overall beam attenuation on the concentration profile. In our calculation framework, this is the contribution from first order of perturbation theory: zeroth order is overall attenuation due to the planarly-averaged loss tangent, and the first order term, which depends on the inhomogeneity in the loss tangent, captures diffraction. Due to the relatively weak absorption of all species in the photoresist, diffraction effects are overall quite negligible, with changes on the order of 0.1 nm on line widths $\sim 10-100$ nm, even at depths of $10-20$ μm. However, since the computational cost of including diffraction is trivial in our framework, we include this effect implicitly in all calculations shown below.

The magnitude of these effects also depends on the overall ratio of intensities between the activating and

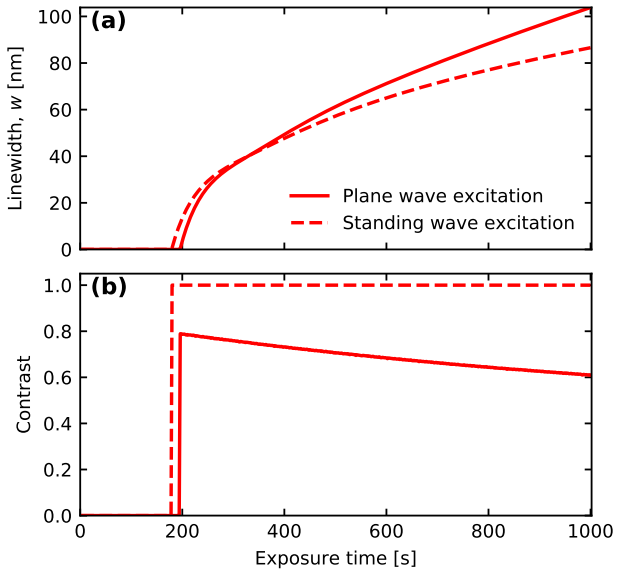

Figure 5: (a) Line width and (b) concentration contrast as a function of exposure times for two configurations of the excitation: plane wave and standing wave (with standing wave inhibition in both cases). Plane wave excitation achieves similar line widths and comparable concentration contrasts as the more complex standing-wave excitation at low exposure times, but the line width increases and contrast decreases with increasing exposure times.

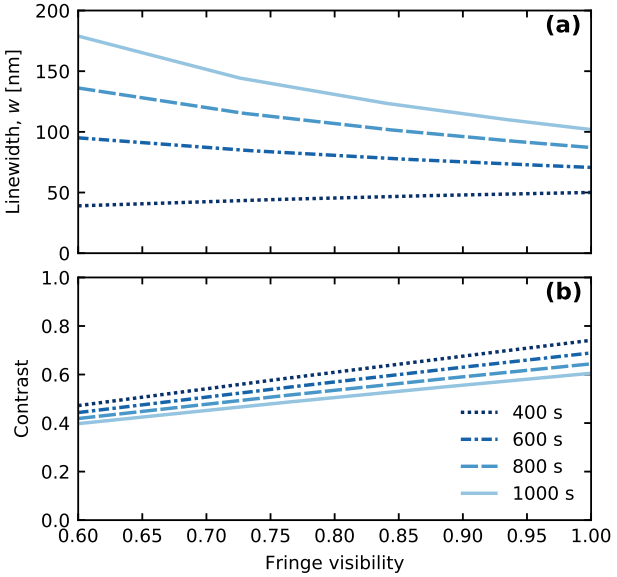

Figure 6: (a) Line width and (b) concentration contrast as a function of the fringe visibility of the inhibition (green) laser standing wave pattern at a few selected exposure times (increasing in color intensity). Concentration contrast decreases when the fringe visibility reduces from the perfect standing wave (visibility = 1).

inhibiting colors. Increasing both intensities and reducing exposure times by the same factor should lead to almost the same concentration profile, as long as the thermal reverse reaction rate (κ in Fig. 1) is negligible. Consequently, we keep I_1 constant and explore the effect of varying the intensity I_2 of the green standing wave. Fig. 4(a) shows that the overall line widths decrease with increasing inhibition intensity I_2 as expected, and this can be compensated by increasing the exposure time. The impact of diffraction is once again negligible throughout, as shown in Fig. 4(b). Depending on experimental constraints of accuracy in controlling exposure times and intensities, it is possible to select reasonable combinations of the two parameters. In the following, we fix $I_2 = 1$ mol/m^2 of photons which allows controlling the line width up to half the standing wave pitch of 130 nm on the time scale of minutes.

Beam modulation effects

Precisely controlling phase and intensities of the interfering beams is critical in interference lithography. Imperfections in the interference pattern lead to poor and spatially varying fringe visibility, which are directly associated with reduced contrast and non-uniform line widths.[22]

Two-color super-resolution interference lithography presents additional challenges, especially in the ideal configuration of standing wave patterns for *both* the excitation and inhibition beams, with maxima of the excitation light coinciding with minima of the inhibition pattern, and vice versa.[18] However, achieving and maintaining precise phase control between two beams of different wavelengths is extremely challenging.

Figure 5 compares the performance of this ideal situation with a much easier configuration that uses a standing wave only for the inhibition, with a plane wave excitation that just uniformly illuminates the whole sample instead. We find that the simpler method performs comparably in terms of both line width and concentration contrast for low exposure times up to about 400 s. The more complex two-standing-wave scheme achieves perfect concentration contrast for all exposure times (Figure 5(b)) because the standing wave excitation ensures zero writing ($C_{\mathrm{MAP}} = 0$) at its nodes. In comparison, in the simpler configuration, SP is activated everywhere and eventually produces MAP everywhere, with the concentration modulated only by the inhibiting beam. Consequently, the contrast in this scheme decreases with increasing exposure time from 80% at 200 s to about 60% at 1000 s.

The above results show that it is possible to work with the much simpler single standing wave pattern, guided by simulations to pick appropriate combinations of intensities and exposure times. Figure 6 further explores the sensitivity of these results to imperfections in the standing wave pattern, as measured by the fringe visibility ($\equiv (I_{\max} - I_{\min})/(I_{\max} + I_{\min})$). When the fringe visibility < 1, the nodes of the inhibiting standing wave are imperfect, leading to some amount of inhibition ev-

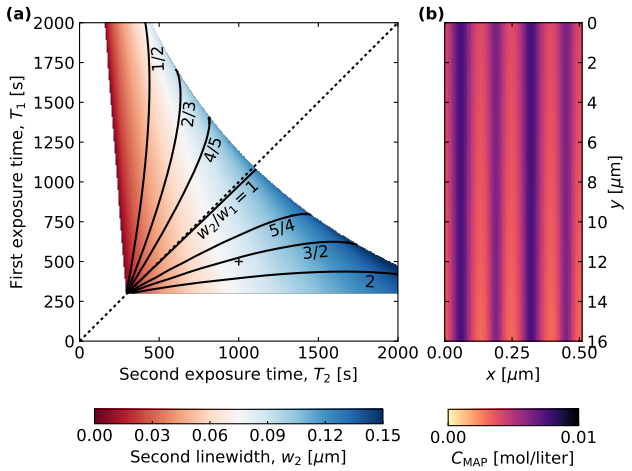

Figure 7: Reducing line spacing by two sequential exposures with shifted standing wave patterns. (a) Ratio of line widths (contours) from the two exposures as a function of the two exposure times, with the color indicating the second line width. Note that equal line width ($w_2/w_1 = 1$) requires slightly different exposures due to the modified initial concentration profile for the second exposure. The empty regions at short exposure times correspond to $C_{\mathrm{map}} < C_0$ everywhere, while those at long exposure times correspond to $C_{\mathrm{map}} > C_0$ everywhere (saturation). (b) Example concentration profile with unequal widths after 500 s and 1000 s exposures (marked + on (a)).

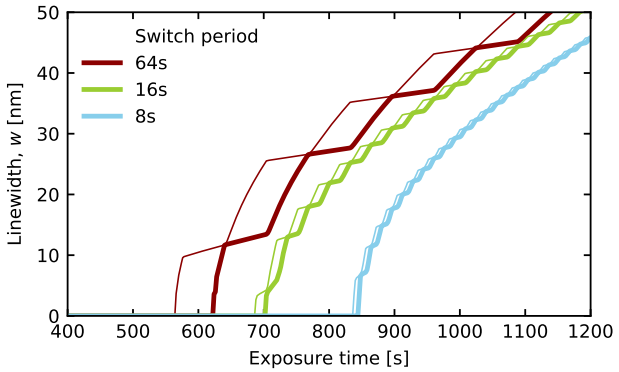

Figure 8: Reducing line spacing by interleaved exposures switching back and forth between shifted standing wave patterns with different time intervals. Thinner lines correspond to w_1 while thicker lines to w_2. The two line widths are nearly equal after each period of the switch, even for switching periods exceeding a minute.

erywhere, thereby reducing contrast. Indeed, Fig. 6(b) shows that the contrast decreases almost linearly with decreasing fringe visibility. Fortunately, a 2% error in the interference pattern (visibility = 0.98), which is easily achievable in practice, only introduces a 1.6% reduction in contrast and 1.2% increase in line width. In particular, the effect of reduced fringe visibility is to increase the inhibition intensity at the minima where the lines first begin to form, and decrease intensity near the maxima where the polymer is generated last. This has the effect of making narrow lines at short exposure times narrower, and broad lines at longer exposure times broader. Overall this leads to less sensitivity of the line widths to fringe visibility at shorter exposure times (400 s and 600 s cases in Fig. 6(a)). Thus shorter exposure times are desirable for their insensitivity to both diffraction effects and imperfections in the interference.

Pitch reduction by multiple exposures

Super-resolution interference lithography allows controlling the width of lines, or size of features more generally, by adjusting the intensities and exposure times as shown above. However, the spacing between features such as the pitch of the line pattern for the present case is limited by the periodicity of the standing wave intensity, which depends on the wavelength ($\sim \lambda/2$). This limitation can be overcome by sequential exposures with shifted interference patterns to write multiple features within the original pitch, taking advantage that the inhibition is reversible and deactivated regions can be reused for writing.

For definiteness, consider the specific case of doubling the resolution or halving the pitch by writing identical lines in a second exposure halfway between those of the first exposure. In this case after a first exposure of time T_1, the phase of one of the two beams in the green standing wave is changed by π for a second exposure of time T_2. Figure 7 shows the phase space of all possible T_1 and T_2 leading to several combinations of widths w_1 and w_2 of the first and second array of lines. To obtain a uniform pattern, $T_2 < T_1$ because the second exposure starts with $C_{\mathrm{MAP}} > 0$ at the end of the first exposure. A minimum time is required for both exposures to get finite width of $C_{\mathrm{MAP}} > C_0$, but after some combined exposure time the entire region gets flooded with $C_{\mathrm{MAP}} > C_0$ removing the pattern.

As discussed above, getting equal lines requires coordination of slightly different first and second exposure times to get uniformity. We explore an alternative strategy that guarantees equal lines: periodically switching back and forth between the two exposure phases at some time interval. Figure 8 shows the evolution of w_1 and w_2 with exposure time in this scheme. Note that w_1 increases sharply while w_2 stays roughly constant when the standing wave is in the first position, while the situation reverses when the standing wave is in the second position. After equal periods in both positions, w_1 and w_2 are nearly identical (visually indistinguishable on the plot), even for relatively large switching times exceeding minutes that are easy to achieve experimentally.

Conclusions

We have implemented an accurate and efficient coupled electromagnetic-reaction kinetics model to inves-

tigate the impact of attenuation, diffraction and intensity modulation on the concentration profiles generated in two-color super-resolution interference lithography. This approach uses a perturbative calculation of electromagnetic wave propagation through patterned photoresist to reduce computational cost by several orders of magnitude compared to FDTD simulations, making it possible to incorporate self-consistent EM solution within a chemical kinetics solver. We find that attenuation has minimal impact for depths ~ 10 μm, especially for short exposure times, while diffraction effects due to spatially non-uniform absorption are virtually negligible. These conclusions remain relatively unchanged over a range of exposure times and laser intensity combinations, providing significant flexibility in experimental realization of desired line widths.

The simulations elucidate simpler experimental configurations using standing wave for only the inhibition beam with comparable performance to the more complex traditional configuration of standing wave for both wavelengths. We find that the simpler configuration with a plane wave excitation illuminating the entire sample can lead to a concentration contrast of up to 80% for short exposure times. This configuration is also relatively insensitive to imperfections in the interference pattern with fringe visibility reductions on the order of 2% only changing the line widths and concentration contrasts by $1 - 1.5\%$.

Finally, we evaluate two alternative schemes for creating features with sub-wavelength spacing in super-resolution interference lithography. Using sequential exposures with shifted standing wave patterns can produce features within the pitch of a single exposure, but require selection of unequal exposure times to compensate for the different starting conditions of the second exposure. Interleaved multiple exposures with practically convenient switch times of few seconds to minutes provides an attractive alternative that results in virtually identical features from the multiple exposures.

The approach established here enables rational design of optical and chemical configurations as well as exposure schemes for two-color super-resolution interference lithography. The EM perturbative approach demonstrated holds promise beyond the insight that it has already provided into the kinetics of spirothiopyran based photoresists, the only super-resolution resist designed to date to have a sufficiently low absorption coefficient to permit high throughput nano-patterning throughout the volume of thick films. Since such nanopatterning is predicated on the resist having a small loss tangent, the perturbative approach is ideal for understanding the coupled optical and chemical dynamics of future two-color photoresists, prime candidates for which are other low threshold super-resolution systems.[7,18] Future work will extend this approach without significant overhead in computational costs to more complex multi-beam interference patterns in three dimensions.

Acknowledgments

This work was supported by the National Science Foundation under Grant No. 1610783 and start-up funding from the Department of Materials Science and Engineering at Rensselaer Polytechnic Institute. Calculations were performed at the Center for Computational Innovations at Rensselaer Polytechnic Institute.

References

(1) Tumbleston, J. R.; Shirvanyants, D.; Ermoshkin, N.; Janusziewicz, R.; Johnson, A. R.; Kelly, D.; Chen, K.; Pinschmidt, R.; Rolland, J. P.; Ermoshkin, A. et al. Continuous Liquid Interface Production of 3D Objects. *Science* **2015**, *347*, 1349–1352.

(2) Walker, D. A.; Hedrick, J. L.; Mirkin, C. A. Rapid, Large-Volume, Thermally Controlled 3D Printing Using a Mobile Liquid Interface. *Science* **2019**, *366*, 360–364.

(3) Liddle, J. A.; Gallatin, G. M. Nanomanufacturing: A Perspective. *ACS Nano* **2016**, *10*, 2995–3014.

(4) Kotz, F.; Risch, P.; Helmer, D.; Rapp, B. E. High-Performance Materials for 3D Printing in Chemical Synthesis Applications. *Advanced Materials* **2019**, *31*, 1805982.

(5) Hell, S. W. Nanoscopy with Focused Light (Nobel Lecture). *Angewandte Chemie International Edition* **2015**, *54*, 8054–8066.

(6) Li, L.; Gattass, R. R.; Gershgoren, E.; Hwang, H.; Fourkas, J. T. Achieving $\lambda/20$ Resolution by One-Color Initiation and Deactivation of Polymerization. *Science* **2009**, *324*, 910–913.

(7) Scott, T. F.; Kowalski, B. A.; Sullivan, A. C.; Bowman, C. N.; McLeod, R. R. Two-Color Single-Photon Photoinitiation and Photoinhibition for Subdiffraction Photolithography. *Science* **2009**, *324*, 913–917.

(8) Fischer, J.; Wegener, M. Ultrafast Polymerization Inhibition by Stimulated Emission Depletion for Three-Dimensional Nanolithography. *Advanced Materials* **2012**, *24*, OP65–OP69.

(9) Buchegger, B.; Kreutzer, J.; Plochberger, B.; Wollhofen, R.; Sivun, D.; Jacak, J.; Schütz, G. J.; Schubert, U.; Klar, T. A. Stimulated Emission Depletion Lithography with Mercapto-Functional Polymers. *ACS Nano* **2016**, *10*, 1954–1959.

(10) Hell, S. W. Strategy for Far-Field Optical Imaging and Writing Without Diffraction Limit. *Physics Letters A* **2004**, *326*, 140–145.

(11) Liaros, N.; Fourkas, J. T. Ten Years of Two-Color Photolithography. *Opt. Mater. Express* **2019**, *9*, 3006–3020.

(12) Liu, Z.-W.; Wei, Q.-H.; Zhang, X. Surface Plasmon Interference Nanolithography. *Nano Lett.* **2005**, *5*, 957–961.

(13) Liu, H.; Luo, Y.; Kong, W.; Liu, K.; Du, W.; Zhao, C.; Gao, P.; Zhao, Z.; Wang, C.; Pu, M. et al. Large Area Deep Subwavelength Interference Lithography with a 35 nm Half-Period Based on Bulk Plasmon Polaritons. *Opt. Mater. Express* **2018**, *8*, 199–209.

(14) Vijayamohanan, H.; Palermo, E. F.; Ullal, C. K. Spirothiopyran-Based Reversibly Saturable Photoresist. *Chemistry of Materials* **2017**, *29*, 4754–4760.

(15) Lu, C.; Lipson, R. H. Interference Lithography: A Powerful Tool for Fabricating Periodic Structures. *Laser Photonics Reviews* **2010**, *4*, 568–580.

(16) Ullal, C. K.; Maldovan, M.; Wohlgemuth, M.; Thomas, E. L.; White, C. A.; Yang, S. Triply Periodic Bicontinuous Structures Through Interference Lithography: A Level-Set Approach. *J. Opt. Soc. Am. A* **2003**, *20*, 948–954.

(17) Graus, P.; Möller, T. B.; Paul, L.; Boneberg, J.; Polushkin, N. I. Direct Laser Interference Patterning of Nonvolatile Magnetic Nanostructures in $Fe_{60}Al_{40}$ Alloy via Disorder-Induced Ferromagnetism. *Opto-Electronic Advances* **2020**, *3*, 190027.

(18) Andrew, T. L.; Tsai, H.-Y.; Menon, R. Confining Light to Deep Subwavelength Dimensions to Enable Optical Nanopatterning. *Science* **2009**, *324*, 917–921.

(19) Vijayamohanan, H.; Kenath, G. S.; Palermo, E. F.; Ullal, C. K. Super-resolution Interference Lithography Enabled by Non-equilibrium Kinetics of Photochromic Monolayers. *RSC Adv.* **2019**, *9*, 28841–28850.

(20) Miller, D. B.; Forman, D. L.; Jones, A. M.; McLeod, R. R. Super-Resolved Critical Dimensions in Far-Field I-Line Photolithography. *Journal of Micro/Nanolithography, MEMS, and MOEMS* **2019**, *18*, 1–10.

(21) Maldovan, M.; Thomas, E. L. *Periodic Materials and Interference Lithography: For Photonics, Phononics and Mechanics*; Wiley, 2008.

(22) Rumpf, R. C.; Johnson, E. G. Fully Three-Dimensional Modeling of the Fabrication and Behavior of Photonic Crystals Formed by Holographic Lithography. *J. Opt. Soc. Am. A* **2004**, *21*, 1703–1713.

(23) Yang, H. F.; He, H. D.; Zhao, E. L.; Han, J.; Hao, J. B.; Qian, J. G.; Tang, W.; Zhu, H. Simulation and Fabrication of Nanostructures with Laser Interference Lithography. *Laser Physics* **2014**, *24*, 065901.

(24) Lin, T.-H.; Yang, Y.-K.; Fu, C.-C. Integration of Multiple Theories for the Simulation of Laser Interference Lithography Processes. *Nanotechnology* **2017**, *28*, 475301.

(25) Vijayamohanan, H.; Bhide, P.; Boyd, D.; Zhou, Z.; Palermo, E. F.; Ullal, C. K. Effect of Chemical Microenvironment in Spirothiopyran Monolayer Direct-Write Photoresists. *Langmuir* **2019**, *35*, 3871–3879.

(26) Oskooi, A. F.; Roundy, D.; Ibanescu, M.; Bermel, P.; Joannopoulos, J.; Johnson, S. G. Meep: A flexible Free-Software Package for Electromagnetic Simulations by the FDTD Method. *Computer Physics Communications* **2010**, *181*, 687–702.

(27) Dormand, J.; Prince, P. A Family of Embedded Runge-Kutta Formulae. *Journal of Computational and Applied Mathematics* **1980**, *6*, 19–26.

(28) Hiemenz, P. C.; Lodge, T. P. *Polymer Chemistry*, 2nd ed.; CRC Press, 2007.

(29) Born, M.; Wolf, E.; Bhatia, A. B.; Clemmow, P. C.; Gabor, D.; Stokes, A. R.; Taylor, A. M.; Wayman, P. A.; Wilcock, W. L. *Principles of Optics: Electromagnetic Theory of Propagation, Interference and Diffraction of Light*, 7th ed.; Cambridge University Press, 1999.

TOC Graphic